

# Gold-Free Ternary III–V Antimonide Nanowire Arrays on Silicon: Twin-Free down to the First Bilayer

Sònia Conesa-Boj,<sup>†</sup> Dominik Kriegner,<sup>‡</sup> Xiang-Lei Han,<sup>§</sup> Sébastien Plissard,<sup>||</sup> Xavier Wallart,<sup>§</sup> Julian Stangl,<sup>‡</sup> Anna Fontcuberta i Morral,<sup>†</sup> and Philippe Caroff<sup>\*,§,⊥</sup>

<sup>†</sup>Laboratoire des Matériaux Semiconducteurs, École Polytechnique Fédérale de Lausanne, 1015 Lausanne, Switzerland

<sup>‡</sup>Institute of Semiconductor and Solid State Physics, Johannes Kepler University Linz, A-4040 Linz, Austria

<sup>§</sup>Institut d'Électronique, de Microélectronique et de Nanotechnologie, UMR CNRS 8520, Avenue Poincaré, C.S. 60069, 59652 Villeneuve d'Ascq, France

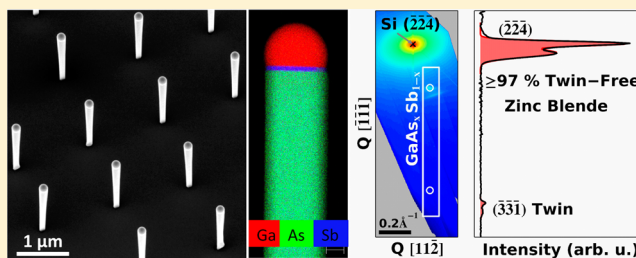
<sup>||</sup>Kavli Institute of Nanoscience, Delft University of Technology, 2628CJ Delft, The Netherlands

<sup>⊥</sup>Department of Electronic Materials Engineering, Research School of Physics and Engineering, The Australian National University, Canberra, ACT 0200, Australia

## Supporting Information

**ABSTRACT:** With the continued maturation of III–V nanowire research, expectations of material quality should be concomitantly raised. Ideally, III–V nanowires integrated on silicon should be entirely free of extended planar defects such as twins, stacking faults, or polytypism, position-controlled for convenient device processing, and gold-free for compatibility with standard complementary metal–oxide–semiconductor (CMOS) processing tools. Here we demonstrate large area vertical GaAs<sub>x</sub>Sb<sub>1–x</sub> nanowire arrays grown on silicon (111) by molecular beam epitaxy. The nanowires' complex faceting, pure zinc blende crystal structure, and composition are mapped using characterization techniques both at the nanoscale and in large-area ensembles. We prove unambiguously that these gold-free nanowires are entirely twin-free down to the first bilayer and reveal their three-dimensional composition evolution, paving the way for novel infrared devices integrated directly on the cost-effective Si platform.

**KEYWORDS:** Nanowire, III–V, antimonide, GaAsSb, crystal structure, silicon, zinc blende, twin-free, transmission electron microscopy, energy dispersive X-ray spectroscopy, molecular beam epitaxy, X-ray diffraction, synchrotron radiation



Among semiconductor materials, III–V compound semiconductors are attractive for high performance application as they combine a direct bandgap with the potential for band-structure engineering and high carrier mobility. Despite renewed interest in III–V integration with the silicon platform, differences in lattice parameters, thermal expansion coefficients, and polar-on-nonpolar nucleation<sup>1–3</sup> led to the development of alternative approaches such as the wafer bonding technique,<sup>4,5</sup> the use of complex pseudo- or metamorphic buffer stacks,<sup>6–9</sup> and nanowire (NW) growth on silicon.<sup>10,11</sup> In this context, the bottom-up option, via gold-seeded binary NWs offers additional potential, with the proven ability in certain material systems to control the crystal structure between pure wurtzite (WZ) and pure zinc blende (ZB).<sup>12–15</sup> Nevertheless, gold introduces disastrous midgap states in silicon and is therefore excluded from silicon fabs and complementary metal–oxide–semiconductor (CMOS) compatible technological processes. Although the successful integration of III–V NWs on silicon has been demonstrated using both self-catalyzed growth and selective area epitaxy,<sup>16–18</sup> reports of crystal phase purity are

rare for binary materials<sup>19,20</sup> and absent in the case of ternaries.<sup>21–24</sup>

Beginning with the first controlled growths via the gold-assisted vapor–liquid–solid mechanism,<sup>25–28</sup> antimonide nanowires have always been observed to exhibit a twin-free ZB structure. This exceptional crystal perfection couples with unique material properties such as very large carrier mobilities,<sup>29</sup> all three types of band alignments, and large spin–orbit coupling.<sup>30,31</sup> Therefore, if gold-free ternary antimonide NWs were to preserve their pure crystal phase when grown on silicon, they could represent a significant step forward in integrating III–V functions on silicon (thermovoltaics, thermoelectrics, and photodetection).<sup>32–34</sup> Previous reports of ternary antimonide NW growth have been limited,<sup>35–40</sup> and before our recent work revealing the Raman properties and optical quality of composition-controlled self-

**Received:** November 3, 2013

**Revised:** November 29, 2013

**Published:** December 13, 2013

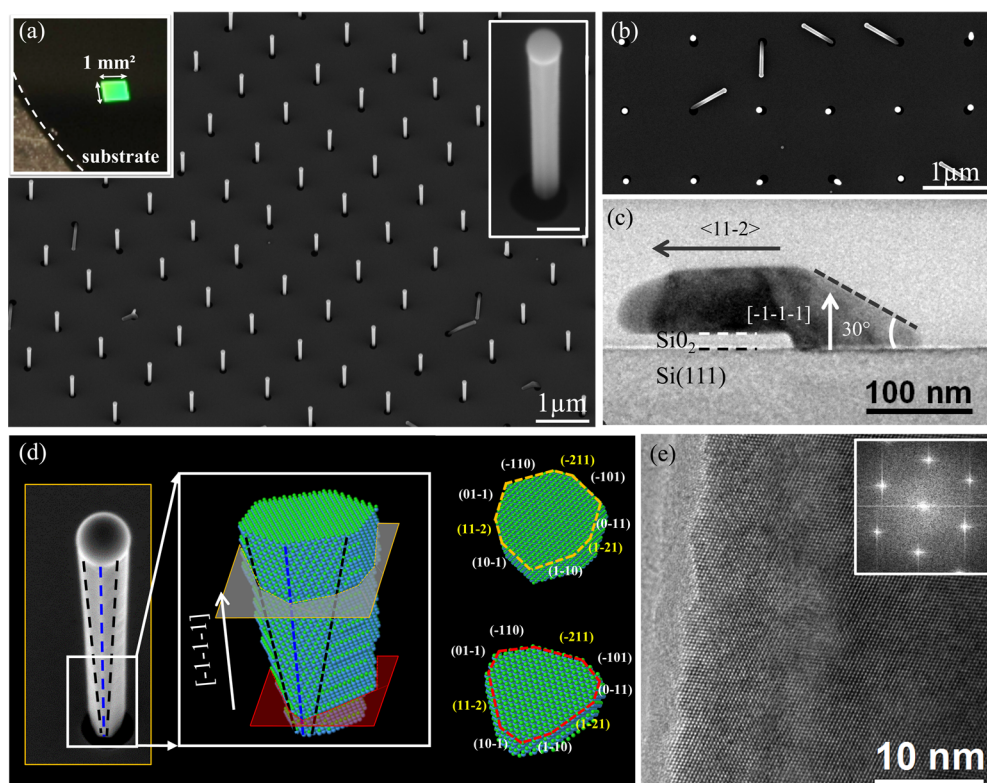


**Figure 1.** (a) SEM image (30° tilt) illustrating  $\text{GaAs}_x\text{Sb}_{1-x}$  NWs grown for 15 min at 630 °C on silicon (111) using an array of  $\sim 130$  nm holes etched in a thermally grown 35 nm thick  $\text{SiO}_2$  mask after standard electron beam lithography; top left inset shows a digital optical photograph of the array, as seen by naked eyes; top right inset shows a high magnification SEM image of a single NW (scale bar is 100 nm). (b) Top view image of the same sample (0° tilt) revealing growth directions for both vertical and nonvertical epitaxial NWs with respect to the substrate; the scale bar is 1  $\mu\text{m}$ . (c) Low-magnification TEM image of one of the nonvertical NWs showing its growth direction to be along  $\langle 11-2 \rangle$ ; the white arrow shows the  $[-1-1-1]$  vertical direction. (d) High-magnification SEM image of a single NW and associated 3D model revealing the complex faceting composed of  $\{110\}$  and  $\{112\}$  planes. (e) High-resolution TEM image taken along a  $[0-11]$  zone axis of a typical NW showing pure twin-free zinc blende crystal structure. Nanofaceting is visible on the side of the NW. The inset shows the fast Fourier transform pattern, typical of untwinned zinc blende.

catalyzed  $\text{GaAs}_x\text{Sb}_{1-x}$  NWs grown on silicon,<sup>41</sup> only axial heterostructures were reported.<sup>42–45</sup>

In this work we report the growth of large area gold-free ternary antimonide NW arrays on silicon. After revealing their external nanofaceting, we study their internal crystal structure and three-dimensional composition evolution both at the single NW level and in large ensembles. It is found that the  $\text{GaAs}_x\text{Sb}_{1-x}$  NWs grow via a self-catalyzed vapor–liquid–solid (VLS) mechanism with a large quantity of antimony present in the Ga droplet during growth. Importantly, we prove unambiguously that the vast majority of NWs (at least 97%) are pure twin-free ZB crystals down to the first nucleation event, across the entire square millimeter array. Their three-dimensional composition evolution is thoroughly studied, revealing a self-formed core–shell structure with Sb-poor regions at apexes and interfaces.

The NWs were grown by solid source molecular beam epitaxy (MBE) on Si(111) substrates in patterned arrays following electron-beam lithography of a thermally grown  $\text{SiO}_2$  layer (see Supporting Figure S1 for the processing details and ref 46). The substrate temperature was ramped directly to 630 °C, without an annealing step, and growth was initiated by opening the three fluxes ( $\text{As}_4$ ,  $\text{Sb}_2$ , and Ga) simultaneously. Growth proceeded for periods of between 15 and 60 min depending on the sample was terminated by switching off all fluxes simultaneously and was followed by cooling to 200 °C within minutes. The NW nucleation and crystal structure was

monitored in situ by using reflection high energy electron diffraction (RHEED) throughout the entire procedure. Once the temperature had been fixed, it was found that V/III ratio is the main parameter controlling successful NW nucleation, diameter, composition, growth rate, shape, and faceting (see ref 41 for more details about morphological and compositional control). High-resolution transmission electron microscopy (TEM) images and energy dispersive X-ray spectroscopy (EDX) analyses were obtained using a FEI Tecnai OSIRIS microscope operated at 200 kV, equipped with a Super-X (0.9 rad collection angle) detector. The indexing adopted in this work assumes an As-terminated NW growth direction, in line with a recent work by de la Mata et al.<sup>47</sup>

Figure 1a shows a scanning electron microscopy (SEM) image taken from a representative region of a square millimeter large array containing one million  $\text{GaAs}_x\text{Sb}_{1-x}$  NWs grown on Si(111), in a mask with pitch of 1  $\mu\text{m}$  and hole diameter of 130 nm (see Supporting Information, S2 for additional SEM images). The inset in the top left corner shows a digital optical photograph of the array, as seen by naked eyes; the inset in top right corner shows a high magnification SEM image of a single NW from this array. The yield of NWs, taking into consideration both vertical and horizontal NWs, is close to 100%, meaning that each hole supports nucleation of a single NW. All NWs are terminated by metallic droplets, which are still visible after cooling (see inset), an indication that growth occurred by the self-catalyzed vapor–liquid–solid mechanism.

The majority of NWs are seen to have grown in the  $[-1-1-1]$  direction, with a few other directions noted.<sup>48,49</sup> Taking a selection of several thousand NWs the vertical yield, which may be defined as the proportion of NWs growing perpendicular to the substrate relative to the total number of holes is found to be 82.4%. Analysis of the top-view SEM image seen in Figure 1b and the associated low magnification cross-section TEM image made on a nonvertical NW from a similar array (Figure 1c) reveals that these NWs are still epitaxial to the substrate but have kinked at the substrate/mask region and grow horizontally into one of the  $\langle 11-2 \rangle$  directions, which is the projection in the plane of the substrate of one of the three nonvertical  $\langle 111 \rangle$  directions.<sup>50</sup>

Figure 1d shows a SEM image of a representative vertical NW and the corresponding three-dimensional atomic model, revealing their complex morphology (see Supporting Information, S3 for a SEM movie made of successive images, and illustrating their 3D faceting). To better illustrate this morphology in Figure 1d we show two cross sections of the atomic model computed at different points along the NW length. As can be observed, the NW exhibits six  $\{110\}$  and three  $\{112\}$  facets, with the dominating facet type reversing along the length of the NW. The inverse tapering ratio is 8% as measured by TEM. In typical Ga-assisted GaAs NWs, only six  $\{110\}$  facets are present after growth termination.<sup>51</sup> Therefore the presence of the extra  $\{112\}$  facets hints at the presence of concomitant lateral growth, which was shown previously to alter the original hexagonal NW shape.<sup>38,52</sup> The full three-dimensional chemical analysis of the NWs will reveal the origin of the complex faceting later in the text.

To understand the NW crystalline structure, we have analyzed a few tens of NWs by means of high-resolution TEM. A representative high-resolution TEM image of a NW sidewall is illustrated in Figure 1e, with the corresponding fast Fourier transform as inset. In all cases planar defects are found to be absent along the entire nanowire length: the crystalline structure thus being twin-free pure ZB. A twin-free ZB crystal structure was also found for other samples grown with differing antimony concentration (see Supporting Figure S4). This apparent promise of crystal phase perfection is in clear contrast to the majority of published reports on both standard III–V ternary NWs and gold-free NWs grown on silicon. Even when overall “crystal phase perfection” is claimed, structural analysis of the NWs close to their nucleation interface and at their end reveal a detrimental concentration of twins, stacking faults, or even inversion of their crystal structure (WZ/ZB), explained by sensitivity to transients in the growth conditions at growth nucleation and termination.<sup>53–55</sup> These defects can be furthermore easily missed when breaking-off the NWs from their host substrates for TEM analysis. Additional analysis focusing at the NW/substrate interface over a statistically relevant number of NWs was used to determine whether or not the  $\text{GaAs}_x\text{Sb}_{1-x}$  NWs in this work could be considered free of planar defects.

Figure 2a shows a typical RHEED pattern acquired in situ, during NW growth. This signal originates from the diffraction of electrons by NWs growing on the nonpatterned silicon reference (native-oxide covered) substrate placed at the center of our sample holder and coinciding with the RHEED spot central position in our MBE system. In the configuration where the RHEED source is aligned to a  $\langle 110 \rangle$  zone axis (analogous to a  $\langle 110 \rangle$  zone axis TEM diffraction pattern), we observe a single zinc-blende set of diffraction spots. This is remarkable

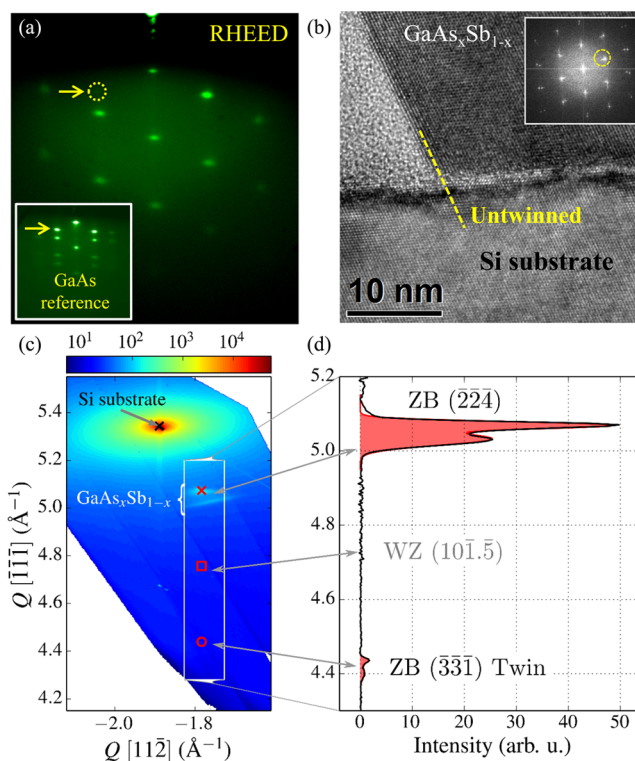


**Figure 2.** (a) Typical RHEED diffraction pattern during  $\text{GaAs}_{1-x}\text{Sb}_x$  NW growth, and diffraction pattern for a reference GaAs NWs as inset. (b) High-resolution TEM image of the  $\text{GaAs}_x\text{Sb}_{1-x}/\text{Si}$  interface and associated fast Fourier transform as the inset, revealing the perfect epitaxial relationship:  $(-1-1-1)[01-1]_{\text{GaAs}_x\text{Sb}_{1-x}} \parallel (111)[01-1]_{\text{Si}}$  and differences in lattice parameters. The yellow line illustrates the epitaxial relationship. (c) X-ray diffraction reciprocal space map showing the diffracted intensity around an asymmetric  $(-2-2-4)$  Bragg reflection, on a logarithmic scale, for the  $\text{GaAs}_x\text{Sb}_{1-x}$  NW array illustrated in Figure 1a. (d) Ensemble averaged intensity distribution of the ZB  $(-3-3-1)$  twin/ZB $(-2-2-4)$  and WZ  $(10-1-5)$  reflections showing that the vast majority of NWs grows untwinned.

since in other ZB NW systems two twin orientations are visible at all times (see for instance a typical Ga-assisted GaAs NW growth as inset on the bottom left of Figure 2a). Indeed, due to the fact that the RHEED diffraction pattern forms on the fluorescent screen from the diffraction of a large number of NWs, single or multiple twins, forming at any position in the NW will give rise to a double-spot pattern characteristic of a twinned material. To investigate this further, cross-section lamellae were prepared using a standard focused ion beam technique along the NW vertical direction (see Supporting Figure S5 for an overview of lamella and additional TEM images of the interface). A high-resolution TEM image of this interface is shown in Figure 2b. For all analyzed NWs from the lamella, the epitaxial relationship to Si was found to be always  $(-1-1-1)[01-1]_{\text{GaAs}_x\text{Sb}_{1-x}} \parallel (111)[01-1]_{\text{Si}}$ , implying that a twin was never formed in this region, even for the first plane at the interface. As a result, in this lamella each of the investigated NWs has the same ZB orientation as all of the others.

To validate this local observation at a larger scale, high-resolution X-ray diffraction (XRD) experiments have been performed in the European Synchrotron Radiation Facility in Grenoble (France), at beamline BM20. An X-ray beam of 0.1078 nm wavelength and with dimensions of  $0.5 \times 2 \text{ mm}^2$



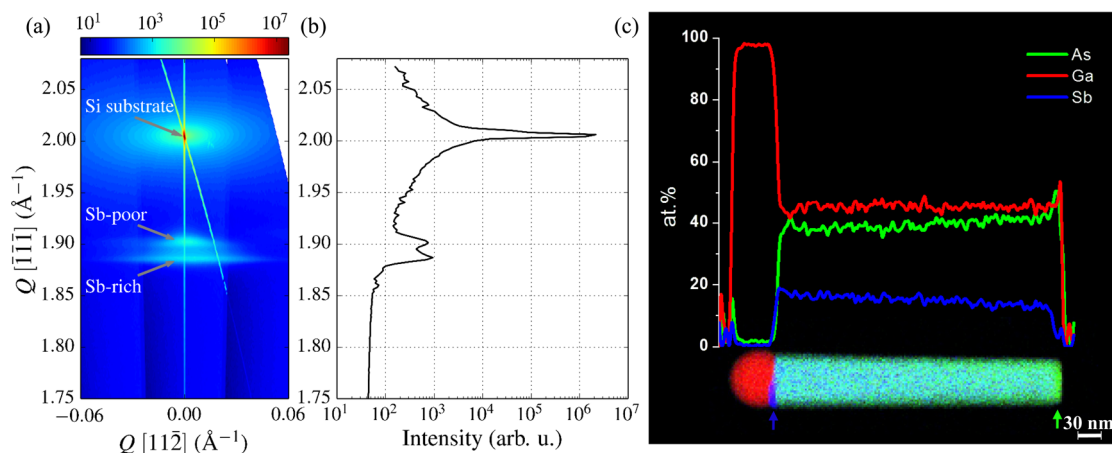


**Figure 3.** (a) X-ray diffraction symmetric reciprocal space maps around the  $(-1-1-1)$  Bragg peak showing the logarithmic scattering intensity. (b) Line scans along the  $[-1-1-1]$  direction, showing clearly the presence of two peaks, corresponding to different antimony concentrations. (c) EDX compositional map of a NW grown in the same run as the large array, but on native-oxide covered Si, showing the signal for Ga, As, Sb, and the associated EDX line scan profile, taken in the center of the NW from bottom to top. Small arrows point at the GaSb-rich segment (blue) at the droplet/NW interface and at an antimony-poor region at the bottom of the NW (green).

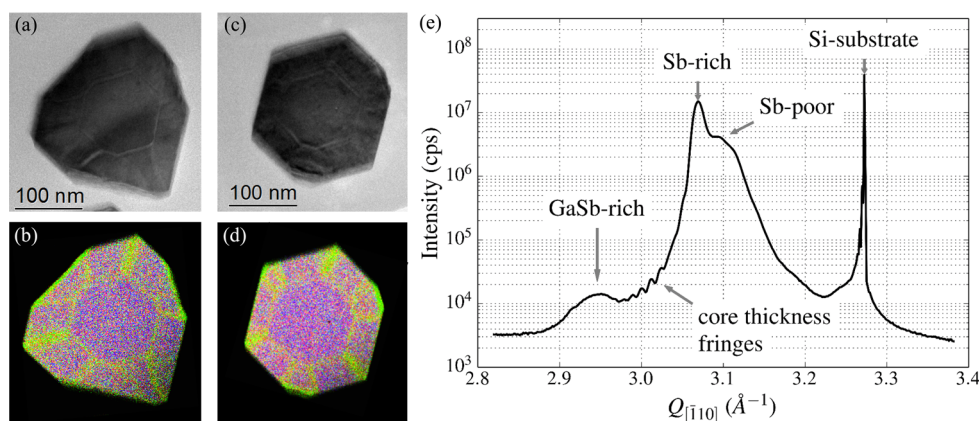


**Figure 4.** (a–d) Cross-section TEM image and associated EDX maps taken at the bottom (a,b) and top regions (c,d) of a NW in the  $[-1-1-1]$  zone axis. The composite EDX map images shows the signal for As (green color), Ga (red color), and Sb (blue color); the yellow/green regions at apexes and interfaces are Sb-poor, with about 10% less Sb than in the violet regions. Note that this sample was grown for 60 min and therefore has larger dimensions than NWs from the array's sample; still qualitative compositional variations are comparable for both samples. (e) Grazing incidence X-ray diffraction radial scan of the  $(2-20)$  Bragg peak, taken on the NW array sample. Visible are the Si substrate and peak and scattering signal of the different parts of the NWs, including thickness oscillations due to the NW core diameter.

was used to record the intensity distribution around several Bragg peaks in reciprocal space. We use the coplanar diffraction geometry as sketched in Supporting Figure S6. Considering the beam footprint at the incidence angle, the full array of NWs is illuminated by the X-ray beam. Figure 2c shows an overview of the intensity distribution around the asymmetric  $(-2-2-4)$  substrate Bragg reflection. Besides an intense peak associated with the Si substrate, a clear double peak is attributed to the  $(-2-2-4)$  reflection from  $\text{GaAs}_x\text{Sb}_{1-x}$ , while a very faint double peak is attributed to the  $(-3-3-1)$  reflection arising only from the associated twin orientation (see Supporting Figure S6b for an illustration of the effect of twinning on the Bragg diffraction positions). Between these two reflections,  $(-2-2-4)$  and  $(-3-3-1)$  TW, the Bragg peak due to wurtzite (WZ)  $\text{GaAs}_x\text{Sb}_{1-x}$  would be expected in the position indicated. To quantify the amount of material exhibiting each orientation, the intensity is integrated along the  $[11-2]$  direction in Figure 2d within the area marked by the rectangle in panel c. After the subtraction of diffuse background scattering, the peaks linked to untwinned and twinned  $\text{GaAs}_x\text{Sb}_{1-x}$  material are visible. Fitting

the diffraction peak areas and considering the different reflection strengths, we conclude that at least 97% of the  $\text{GaAs}_x\text{Sb}_{1-x}$  material is ZB of the same orientation as the substrate. The remainder is ZB of the twinned orientation with no WZ material being detected. The observed double peak structure will be discussed later in the text. Since TEM measurements prove that detached NWs are free of twins and stacking faults away from the interface, this indicates unambiguously that, even on a macroscopic scale, the NW array is largely twin-free throughout the entire length of the NWs.

Figure 3a shows an X-ray diffraction symmetric reciprocal space map for the NW array. In addition to the peak attributable to the silicon substrate, the signal attributable to  $\text{GaAs}_x\text{Sb}_{1-x}$  reveals not one but two peaks with an intensity distribution as illustrated in Figure 3b. These double peaks were also observed by analyzing another sample with a different nominal antimony composition (see Supporting Figure S7). While the orientation and lattice spacing of the  $\{111\}$  lattice planes may be obtained from the symmetric reciprocal space

maps presented in Figure 3a, a strain state can be extracted from the asymmetric reciprocal space map,<sup>56</sup> with an in-plane strain below 0.15% being found for both peaks. Assuming a biaxial strain configuration and using lattice spacing information, a chemical composition may be ascribed to these features, with values of around  $x_{\text{Sb}} = 0.17$  and  $x_{\text{Sb}} = 0.29$ . It should be noted that small deviations from ideal biaxial strain would only marginally affect these extracted values. Such a bimodal distribution of composition could be representative of differences between nanowire types (vertical and horizontal) or compositional variation within the nanowires themselves. To investigate this further, a study of both XRD and TEM analyses is performed and presented below.

Figure 3c shows an energy-dispersive X-ray spectroscopy (EDX) map, with signals characteristic of As, Ga, and Sb for a representative nanowire (see Supporting Figure S4c for a similar analysis performed on samples with different antimony concentrations). A small Sb-rich segment at the NW/droplet interface (highlighted by a small blue arrow) is observed likely indicating that the Ga seed contains a large proportion of Sb during growth. When terminating growth in the absence of a group V flux at the high temperature chosen for growth (630 °C), arsenic is expected to be nearly instantaneously removed from the growth front with the nucleation of a GaSb-rich segment likely following during cool down. After cooling, no antimony is found in the Ga droplet. We further note that the nucleation of a short segment from Sb stored in the particle has already been inferred for the termination of In-seeded InSb wires.<sup>57</sup> At the base of the nanowire another minor compositional inhomogeneity is observed (highlighted by a small green arrow), where for less than 20 nm the NW is relatively Sb-poor (see the line scan profile). As antimony and arsenic are provided simultaneously at nucleation, this transient composition could be due to either the necessity for antimony to reach a higher steady-state concentration in the droplet before being incorporated or to a substrate effect, where the antimony and arsenic diffusion lengths are expected to differ. Looking at the EDX line scan in Figure 3c, the antimony concentration slowly increases from the base to the tip of the NW. The origin of this variation will become clear in Figure 4. None of these sources of compositional inhomogeneity can however account for the double peak in the X-ray diffraction data. Both the GaSb-rich island at the top and small Sb-poor region at the base of the NW have relatively small volumes (see Figure 4e for a signature of the GaSb-rich segment using the grazing incidence diffraction geometry), while the linear variation in antimony concentration would be expected to generate a single smeared XRD signal rather than the two distinct peaks.<sup>56</sup> We thus consider core-shell formation, as may be inferred from the original faceted shape of the NW, illustrated in Figure 1.

Cross sections lamella were prepared perpendicular to the NW axis for TEM analysis (see Supporting Figure S5 for an overview of the TEM lamella). Figure 4 illustrates two typical cross sections originating from the bottom (a, b) and top regions (c, d) of the NWs, respectively. The compositional EDX mapping of these NW cross sections clearly confirms the presence of both a core and shell. Note that the Sb-poor regions (with reduced Sb concentration by about 10%) of the shell are facet-dependent, in agreement with recent studies showing the crucial role of polarity in core-shell composition variations.<sup>58–60</sup> As NWs grow axially via the VLS mechanism, concomitant radial growth occurs on the NW's sidewall facets. From the presence of an antimony-poor signal at the interface

between core and shell, the diameter evolution of both core and shell can be understood. Comparing Figure 4b and d reveals that the core diameter does not significantly change along the growth axis while the shell morphology is continuously evolving from a triangular toward a hexagonal shape. The global (core+shell) NW diameter is slightly inversely tapered with a diameter change of about 8% from bottom to top. The changing core-shell geometry can also be inferred from perpendicular EDX line scans, taken at different heights of a NW from the same run as the array (see Supporting Figure S8). It is clear that the observed slow increase of the Sb concentration, shown in Figure 3c, is thus due to this core-shell evolution. Since the variation of the core diameter along the wire axis and within the ensemble of NWs is small, it leads to the thickness fringes observed in the grazing incidence X-ray diffraction measurements shown in Figure 4e. In light of this observation, one could postulate that the origin of the double peaks in the XRD data could lie in the different average Sb-composition in the core and shell, giving rise to spatially separated Sb-poor and Sb-rich regions. However, this scenario would require plastic relaxation in the  $[-1-1-1]$  direction, with related misfit dislocations at approximately every 20–40 nm along the core-shell interface. We have, however, not found any dislocations at the core-shell interface using high-resolution TEM, both in cross section measurements and in measurements along the nanowire diameter (see Supporting Figure S9 and S10). Given the exhaustive TEM analysis it is unlikely that we would have missed dislocations in a density required to explain the XRD measurements. Another suggestion is that the lower Sb peak could instead originate from the contribution of the nonvertical  $\langle 11-2 \rangle$ -oriented nanowires. This would mean that the signal labeled Sb-rich in Figure 3a originates from the vertical nanowires, whereas the signal labeled Sb-poor originates from the horizontal NWs. The fact that the ratio of the measured peak intensities does not correlate directly with the ratio of vertical to nonvertical nanowires (82.4%/17.6%) could seem surprising. As the tilt distributions of the vertical and nonvertical nanowires is however clearly different and the X-ray data represents cuts in reciprocal space of these differing tilt distributions, the relative peak intensities cannot therefore be related in a quantitative manner to the relative scattering volumes. This uncertainty does not extend to the determined ratio between twin-orientations since that signal originates from structures with the same tilt orientation. Careful inspection of the positions along  $[11-2]$  of the peaks labeled "Sb-rich" and "Sb-poor" in Figure 3a (more clearly visible in Figure S7) reveals not only a differing tilt distribution, but also a difference in the average tilt of the scattering objects. It is very unlikely that a core-shell structure could give rise to such a difference in tilt, which supports our assignment of the double peak feature to the vertical and nonvertical wires, respectively. In the determination of chemical composition from the diffraction peak positions, these tilts have already been taken into account. The obtained values correspond very well to the EDX measurements of vertical and nonvertical NWs giving Sb compositions of 27% and 17%, respectively (see Supporting Figure S11). Therefore the analysis in Supporting Figure S11 clearly favors the second scenario in which the two peaks in the X-ray diffraction data arise from different nanowires from the same array. That such a compositional difference may be linked to growth direction illustrates the richness of effective parameters affecting

nanoscale alloying in ternary nanowires and could lead to original methods of compositional control.

In conclusion, we have grown for the first time ternary antimonide NWs arrays directly on silicon and shown they could be obtained with high vertical yield and excellent morphological homogeneity. We studied their structural and chemical composition with advanced TEM and XRD techniques and methodologies. By combining RHEED, TEM, and XRD, we have proven the highest level of structural quality in a NW ensemble, over a macroscopic scale. Interestingly, the complexity of the fully 3D elemental distribution illustrated in our work opens up new challenges both in terms of fundamental growth mechanism understanding and for practical design of high quality device-focused ternary alloys.

## ■ ASSOCIATED CONTENT

### ■ Supporting Information

Process flowchart for the arrays, S1. Additional SEM images of the NW array from Figure 1, S2. Representative 3D morphology of a single NW, including a movie, S3. Compositional tunability as a function of the Sb flux, and associated crystal structure, S4. TEM cross-section preparation and additional images, S5. Sketch of the coplanar XRD geometry, S6. XRD line scan from another NW array showing again the double-peak feature and more details about these experiments, S7. EDX line scans perpendicular to the NW growth direction, S8. Analysis of the core-shell interface in the  $[-1-1-1]$  zone axis, S9. Analysis of the core-shell interface in the  $[0-11]$  zone axis, S10. EDX analysis of a nonvertical NW: lower Sb concentration than in vertical NWs, S11. This material is available free of charge via the Internet at <http://pubs.acs.org>.

## ■ AUTHOR INFORMATION

### Corresponding Author

\*E-mail: philippe.caroff@anu.edu.au;

### Notes

The authors declare no competing financial interest.

## ■ ACKNOWLEDGMENTS

This work was performed within the Institut d'Électronique, de Microélectronique et de Nanotechnologie, Centre National de la Recherche Scientifique (IEMN, UMR CNRS 8520), and within the Laboratoire des Matériaux Semiconducteurs from Ecole Polytechnique Fédérale de Lausanne. P.C. acknowledges David Troadec for FIB preparation of the TEM lamella, Emilie Caroff for help with the NW statistics and Tim Burgess for suggestions and for proof-reading the manuscript. P.C. also acknowledges the French National Research Agency (ANR), TERADOT project, for funding under contract number ANR-11-JS04-002-01 and the Australian Research Council (ARC), Future Fellowship project number FT120100498. S.C.-B. and A.F.i.M. acknowledge funding from the European Research Council (ERC), Starting Grant "Upcon", the NCCR on "Quantum Science and Technology", and a Marie-Heim Vögtlin fellowship from the SNSF. We acknowledge the beamline support at BM20 and ID01 (ESRF, Grenoble). The work was supported by Austrian Academy of Sciences (DOC scholarship of D.K.) and FWF, Vienna (P23706-N19).

## ■ REFERENCES

(1) Kroemer, H. *J. Cryst. Growth* **1987**, *81*, 193–204.

- (2) Fang, S. F.; Adomi, K.; Iyer, S.; Morkoç, H.; Zabel, H.; Choi, C.; Otsuka, N. *J. Appl. Phys.* **1990**, *68*, R31.
- (3) Bolkhovityanov, Y. B.; Pchelyakov, O. P. *Physics* **2008**, *51*, 437–456.
- (4) Tong, Q. Y.; Gösele, U. *Mater. Chem. Phys.* **1994**, *37*, 101–127.
- (5) Fontcuberta i Morral, A.; Zahler, J. M.; Atwater, H. A.; Ahrenkiel, S. P.; Wanlass, M. W. *Appl. Phys. Lett.* **2003**, *83*, 5413–5415.
- (6) Kwon, O.; Boeckl, J. J.; Lee, M. L.; Pitera, A. J.; Fitzgerald, E. A.; Ringel, S. A. *J. Appl. Phys.* **2006**, *100*, 013103–013110.
- (7) Huang, S. H.; Balakrishnan, G.; Khoshakhlagh, A.; Dawson, L. R.; Huffaker, D. L. *Appl. Phys. Lett.* **2008**, *93*, 071102–071105.
- (8) Reboul, J. R.; Cerutti, L.; Rodriguez, J. B.; Grech, P.; Tournié, E. *Appl. Phys. Lett.* **2011**, *99*, 121113–121116.
- (9) Desplanque, L.; El Kazzi, S.; Coinin, C.; Ziegler, S.; Kunert, B.; Beyer, A.; Volz, W.; Wang, Y.; Ruterana, P.; Wallart, X. *Appl. Phys. Lett.* **2012**, *101*, 142111.
- (10) Mårtensson, T.; Svensson, C. P. T.; Wacaser, B. A.; Larsson, M. W.; Seifert, W.; Deppert, K.; Gustafsson, A.; Wallenberg, L. R.; Samuelson, L. *Nano Lett.* **2004**, *4*, 1987–1990.
- (11) Bakkers, E. P. A. M.; van Dam, J. A.; De Franceschi, S.; Kouwenhoven, L. P.; Kaiser, M.; Verheijen, M.; Wondergem, H.; van der Sluis, P. *Nat. Mater.* **2004**, *3*, 769–773.
- (12) Dick, K. A.; Thelander, C.; Samuelson, L.; Caroff, P. *Nano Lett.* **2010**, *10*, 3494–3499.
- (13) Joyce, H. J.; Wong-Leung, J.; Gao, Q.; Tan, H. H.; Jagadish, C. *Nano Lett.* **2010**, *10*, 908–915.
- (14) Vu, T. T. T.; Zehender, T.; Verheijen, M. A.; Plissard, S. R.; Immink, G. W. G.; Haverkort, J. E. M.; Bakkers, E. P. A. M. *Nanotechnology* **2013**, *24*, 115705.
- (15) Lehmann, S.; Wallentin, J.; Jacobsson, D.; Deppert, K.; Dick, K. A. *Nano Lett.* **2013**, *13*, 4099–4105.
- (16) Mandl, B.; Stangl, J.; Mårtensson, T.; Mikkelsen, A.; Eriksson, J.; Karlsson, L. S.; Bauer, G.; Samuelson, L.; Seifert, W. *Nano Lett.* **2006**, *6*, 1817–1821.
- (17) Tomioka, K.; Motohisa, J.; Hara, S.; Fukui, T. *Nano Lett.* **2008**, *8*, 3475–80.
- (18) Jabeen, F.; Grillo, V.; Rubini, S.; Martelli, F. *Nanotechnology* **2008**, *19*, 275711.
- (19) Krogstrup, P.; Popovitz-Biro, R.; Johnson, E.; Madsen, M. H.; Nygård, J.; Shtrikman, H. *Nano Lett.* **2010**, *10*, 4475–4482.
- (20) Cirlin, G. E.; Dubrovskii, V. G.; Samsonenko, Y. B.; Bouravleuv, A. D.; Durose, K.; Proskuryakov, Y. Y.; Mendes, B.; Bowen, L.; Kaliteevski, M. A.; Abram, R. A.; Zeze, D. *Phys. Rev. B* **2010**, *82*, 035302.
- (21) Shin, J. C.; Lee, A.; Mohseni, P. K.; Kim, D. Y.; Yu, L.; Kim, J. H.; Kim, H. J.; Choi, W. J.; Wasserman, D.; Choi, K. J.; Li, X. *ACS Nano* **2013**, *7*, 5463–5471.
- (22) Tomioka, K.; Yoshimura, M.; Fukui, T. *Nature* **2012**, *488*, 189–192.
- (23) Morkötter, S.; Funk, S.; Liang, M.; Döblinger, M.; Hertenberger, S.; Treu, J.; Rudolph, D.; Yadav, A.; Becker, J.; Bichler, M.; Scarpa, G.; Lugli, P.; Zardo, I.; Finley, J. J.; Abstreiter, G.; Koblmüller, G. *Phys. Rev. B* **2013**, *87*, 205303.
- (24) Zhang, Y.; Aagesen, M.; Holm, J. V.; Jørgensen, H. I.; Wu, J.; Liu, H. *Nano Lett.* **2013**, *13*, 3897–3902.
- (25) Guo, Y. N.; Zou, J.; Paladugu, M.; Wang, H.; Gao, Q.; Tan, H. H.; Jagadish, C. *Appl. Phys. Lett.* **2006**, *89*, 231917.
- (26) Park, H. D.; Prokes, S. M.; Twigg, M. E.; Ding, Y.; Wang, Z. L. *J. Cryst. Growth* **2007**, *304*, 399–401.
- (27) Jeppsson, M.; Dick, K. A.; Wagner, J. B.; Caroff, P.; Deppert, K.; Samuelson, L.; Wernersson, L.-E. *J. Cryst. Growth* **2008**, *310*, 4115–21.
- (28) Caroff, P.; Wagner, J. B.; Dick, K. A.; Nilsson, H. A.; Jeppsson, M.; Deppert, K.; Samuelson, L.; Wallenberg, L. R.; Wernersson, L. E. *Small* **2008**, *4*, 878–82.
- (29) van Weperen, I.; Plissard, S. R.; Bakkers, E. P. A. M.; Frolov, S. M.; Kouwenhoven, L. P. *Nano Lett.* **2013**, *13*, 387–391.
- (30) Nilsson, H. A.; Caroff, P.; Thelander, C.; Larsson, M.; Wagner, J. B.; Wernersson, L.-A.; Samuelson, L.; Xu, H. Q. *Nano Lett.* **2009**, *9*, 3151–3156.



- (31) Pistol, M.-E.; Pryor, C. E. *Phys. Rev. B* **2009**, *80*, 035316.
- (32) Fraas, L. M.; Avery, J. E.; Sundaram, V. S.; Dinh, V. T.; Davenport, T. M.; Yerkes, J. W. *IEEE Conf. Photovoltaic Spec.* **1990**, 190 DOI: 10.1109/PVSC.1990.111616.
- (33) Mingo, N. *Appl. Phys. Lett.* **2004**, *84*, 2652.
- (34) Svensson, J.; Anttu, N.; Vainorius, N.; Borg, B. M.; Wernersson, L.-E. *Nano Lett.* **2013**, *13*, 1380–1385.
- (35) Dheeraj, D. L.; Patriarche, G.; Largeau, L.; Zhou, H. L.; van Helvoort, A. T. J.; Glas, F.; Harmand, J. C.; Fimland, B. O.; Weman, H. *Nanotechnology* **2008**, *19*, 275605.
- (36) Zhou, H.; Pozuelo, M.; Hicks, R. F.; Kodambaka, S. J. *Cryst. Growth* **2011**, *319*, 25–30.
- (37) Borg, B. M.; Dick, K. A.; Eymery, J.; Wernersson, L.-E. *Appl. Phys. Lett.* **2011**, *98*, 113104.
- (38) Xu, T.; Dick, K. A.; Plissard, S.; Nguyen, T. H.; Makoudi, Y.; Berthe, M.; Nys, J.-P.; Wallart, X.; Grandidier, B.; Caroff, P. *Nanotechnology* **2012**, *23*, 095702.
- (39) Ercolani, D.; Gemmi, M.; Nasi, L.; Rossi, F.; Pea, M.; Li, A.; Salviati, G.; Beltram, F.; Sorba, L. *Nanotechnology* **2012**, *23*, 115606.
- (40) Ghalamestani, S. G.; Ek, M.; Ganjipour, B.; Thelander, C.; Johansson, J.; Caroff, P.; Dick, K. *Nano Lett.* **2012**, *12*, 4914–4919.
- (41) Alarcón-Lladó, E.; Conesa-Boj, S.; Wallart, X.; Caroff, P.; Morral, A. F. *Nanotechnology* **2013**, *24*, 405707.
- (42) Plissard, S.; Dick, K. A.; Wallart, X.; Caroff, P. *Appl. Phys. Lett.* **2010**, *96*, 121901.
- (43) Munshi, A. M.; Dheeraj, D. L.; Todorovic, J.; van Helvoort, A. T. J.; Weman, H.; Fimland, B.-O. *J. Cryst. Growth* **2013**, *372*, 163–169.
- (44) Kanungo, P. D.; Schmid, H.; Björk, M. T.; Gignac, L. M.; Breslin, C.; Bruley, J.; Bessire, C. D.; Riel, H. *Nanotechnology* **2013**, *24*, 225304.
- (45) Li, T.; Gao, L.; Lei, W.; Guo, L.; Pan, H.; Yang, T.; Chen, Y.; Wang, Z. *Nanoscale Res. Lett.* **2013**, *8*, 333.
- (46) Plissard, S.; Larrieu, G.; Wallart, X.; Caroff, P. *Nanotechnology* **2011**, *22*, 275602.
- (47) de la Mata, M.; Magen, C.; Gazquez, J.; Utama, M. I. B.; Heiss, M.; Lopatin, S.; Furtmayr, F.; Fernandez-Rojas, C. J.; Peng, B.; Morante, J. R.; Rurali, R.; Eickhoff, M.; Morral, A. F. I.; Xiong, Q. H.; Arbiol, J. *Nano Lett.* **2012**, *12*, 2579–2586.
- (48) Fortuna, S. A.; Li, X. *Semicond. Sci. Technol.* **2010**, *25*, 024005.
- (49) Dowdy, R. S.; Walko, D. A.; Li, X. *Nanotechnology* **2013**, *24*, 035304.
- (50) Uccelli, E.; Arbiol, J.; Magen, C.; Krogstrup, P.; Russo-Averchi, E.; Heiss, M.; Mugny, G.; Morier-Genoud, F.; Nygård, J.; Morante, J. R.; Morral, A. F. *Nano Lett.* **2011**, *11*, 3827–3832.
- (51) Colombo, C.; Spirkoska, D.; Frimmer, M.; Abstreiter, G.; Morral, A. F. *Phys. Rev. B* **2008**, *77*, 155326.
- (52) Plante, M. C.; LaPierre, R. R. *J. Cryst. Growth* **2008**, *310*, 356–363.
- (53) Glas, F.; Harmand, J.-C.; Patriarche, G. *Phys. Rev. Lett.* **2007**, *99*, 146101.
- (54) Shin, J. C.; Choi, K. J.; Kim, D. Y.; Choi, W. J.; Li, X. *Cryst. Growth Des.* **2012**, *12*, 2994–2998.
- (55) Biermanns, A.; Breuer, S.; Trampert, A.; Davydok, A.; Geelhaar, L.; Pietsch, U. *Nanotechnology* **2012**, *23*, 305703.
- (56) Kriegner, D.; Persson, J. M.; Etzelstorfer, T.; Jacobsson, D.; Wallentin, J.; Wagner, J. B.; Deppert, K.; Borgström, M. T.; Stangl, J. *Thin Solid Films* **2013**, *543*, 100–105.
- (57) Mandl, B.; Dick, K. A.; Kriegner, D.; Keplinger, M.; Bauer, G.; Stangl, J.; Deppert, K. *Nanotechnology* **2011**, *22*, 145603.
- (58) Guo, Y.-N.; Burgess, T.; Gao, Q.; Tan, H. H.; Jagadish, J.; Zou, J. *Nano Lett.* **2013**, *13*, 5085–5089.
- (59) Heiss, M.; Fontana, Y.; Gustafsson, A.; Wüst, G.; Magen, C.; O'Regan, D. D.; Luo, J. W.; Ketterer, B.; Conesa-Boj, S.; Kuhlmann, A. V.; Houel, J.; Russo-Averchi, E.; Morante, J. R.; Cantoni, M.; Marzari, N.; Arbiol, J.; Zunger, A.; Warburton, R. J.; Fontcuberta i Morral, A. *Nat. Mater.* **2013**, *12*, 439–444.
- (60) Zheng, C.; Wong-Leung, J.; Gao, Q.; Tan, H. H.; Jagadish, J.; Etheridge, J. *Nano Lett.* **2013**, *13*, 3742–3748.